Nanoscale
Advances

PAPER

View Article Online
View Journal | View Issue

Cite this: *Nanoscale Adv.*, 2023, **5**, 861

Facile synthesis of defect-rich RuCu nanoflowers for efficient hydrogen evolution reaction in alkaline media†

Liang Ji,‡[a] Sai Luo,‡[cd] Lei Li,‡[a] Ningkang Qian,[a] Xiao Li,[c] Junjie Li,[a] Jingbo Huang,[a] Xingqiao Wu, *[e] Hui Zhang *[ab] and Deren Yang [ab]

Received 24th November 2022
Accepted 22nd December 2022

DOI: 10.1039/d2na00840h

rsc.li/nanoscale-advances

Developing high-performance electrocatalysts toward hydrogen evolution reaction (HER) in alkaline media is highly desirable for industrial applications in the field of water splitting but is still challenging. Herein, we successfully synthesized RuCu nanoflowers (NFs) with tunable atomic ratios using a facile wet chemistry method. The Ru_3Cu NFs need only 55 mV to achieve a current density of 10 mA cm^{-2}, which shows ideal durability with only 4 mV decay after 2000 cycles, largely outperforming the catalytic properties of commercial Pt/C. The Ru_3Cu NFs comprise many nanosheets that can provide more active sites for HER. In addition, the introduction of Cu can modulate the electronic structure of Ru, facilitate water dissociation, and optimize H adsorption/desorption ability. Thus, the flower-like structure together with the proper incorporation of Cu boosts HER performance.

Introduction

Hydrogen production *via* electrolytic water splitting is considered a promising technology to meet the growing demands for sustainable and clean energy resources.[1–4] As the heart of scalable hydrogen generation, it is urgent to develop highly active and robust electrocatalysts to drive the hydrogen evolution reaction (HER) on a practical scale.[5] Generally speaking, the reaction rate of HER in an acidic solution is significantly higher than that in an alkaline solution. However, water splitting in acidic media is technologically and commercially hindered by the lack of efficient and low-cost electrocatalysts for oxygen evolution reaction (OER) at the anode electrode.[6] Considering that OER is more feasible in alkaline media, it is important to investigate HER under alkaline conditions for further industrial applications.

Pt-based nanocrystals have been theoretically and experimentally proven to be the most promising HER electrocatalyst owing to their proper H adsorption/desorption energy and low overpotential.[7–10] Unfortunately, because of the large kinetic energy barrier for the water dissociation step, their HER activity in alkaline media is approximately 2 to 3 orders of magnitude lower than that in acidic solution.[11,12] Moreover, the scarcity and high cost of Pt-based catalysts further limit their large-scale commercial applications, which arouses unprecedented research interests in developing economical and effective Pt-free electrocatalysts. Non-Pt-based catalysts, such as Mo-, Co-, Ni- and Cu-based nanocrystals, have been extensively reported,[13–16] but they are still inadequate to meet the urgent demands of high activity and durability.

Recently, Ru-based nanocrystals have received great attention as alternative electrocatalysts for HER owing to their moderate hydrogen bond strength (~65 kcal mol^{-1}) and robust anticorrosion ability.[17,18] However, the weak hydrolytic capacity of Ru is still a major obstacle to limiting its intrinsic activity in alkaline solution. In addition, the strong absorption of OH* species can severely block the adsorption/desorption of H* on Ru.[19,20] To overcome these obstacles, tremendous efforts have been devoted, including structure design, shape control and composition optimization.[21–25] Among them, alloying Ru with a transition metal (*e.g.* Ni, Co, and Cu) offers a great opportunity to reduce the energy barrier for the water dissociation process, which exhibits remarkable enhancement in catalytic activity toward HER.[26–28] For example, incorporating Cu heteroatom into Ru can optimize the adsorption energy of H* on the catalyst through the modulation of the electronic structure caused by the ligand effect, which can benefit the HER process.[29,30]

---

[a] *State Key Laboratory of Silicon Materials and School of Materials Science and Engineering, Zhejiang University, Hangzhou, Zhejiang 310027, People's Republic of China. E-mail: msezhanghui@zju.edu.cn*

[b] *Zhejiang Provincial Key Laboratory of Power Semiconductor Materials and Devices, ZJU-Hangzhou Global Scientific and Technological Innovation Center, Hangzhou, Zhejiang 311200, People's Republic of China*

[c] *Sunrise Power Co., Ltd, Dalian, Liaoning 116024, People's Republic of China*

[d] *Dalian Institute of Chemical Physics, Chinese Academy of Sciences, Dalian, Liaoning 116023, People's Republic of China*

[e] *Institute for Carbon Neutralization, College of Chemistry and Materials Engineering, Wenzhou University, Wenzhou, Zhejiang 325035, People's Republic of China. E-mail: xingqiaowu@wzu.edu.cn*

† Electronic supplementary information (ESI) available. See DOI: https://doi.org/10.1039/d2na00840h

‡ These authors contributed equally to this work.

Apart from alloy engineering, rational controlling the morphology of nanocrystals is another promising approach to tailor the catalytic properties.[31–33] Two-dimensional structure (2D) has drawn much attention owing to the advantages of providing a large surface, exposing more active sites and enhancing the diffusion of electrolytes, which can offer a high possibility to facilitate the catalytic performance.[34–37] In this regard, three-dimensional (3D) nanoflowers comprising the units of 2D nanosheet build blocks have emerged as promising candidates for advanced electrocatalysts owing to their integrated advantages of 3D and 2D structures, such as high porosity, large surface area and corrosion-resistance compared with their counterparts.[38–40] The highly opened flower-like structure facilitates the electron transfer among the reaction intermediates[41,42] and provides additional low-coordinated active sites at their edges, steps, and kinks, which can enhance the HER kinetics.[41,42]

Herein, we report a facile wet chemical method for synthesizing a class of defect-rich RuCu nanoflowers (denote as Ru_xCu NFs) to meet the demands of advanced HER catalysts. Owing to the enhanced active sites originating from the 3D structure and the optimized electronic structure of Ru modulated by incorporation of Cu, the as-synthesized Ru_3Cu NFs show a low overpotential of 55 mV, a Tafel slope of 52.7 mV dec^{-1} and excellent long-term durability. The DFT calculations further indicate that both enhanced water dissociation and H adsorption abilities help improve HER performance, making Ru_3Cu NFs possible for further practical applications.

Experimental section

Materials and chemicals

Ruthenium(III) acetylacetonate ($Ru(acac)_3$, 97%), copper(I) chloride (CuCl, 99%), polyvinylpyrrolidone (PVP, $M_w \approx 29\,000$), L-ascorbic acid ($C_6H_8O_6$, AA), citric acid ($C_6H_8O_7$, CA), glucose (C_6H_6O) and Nafion (5 wt%) were purchased from Sigma-Aldrich. Benzyl alcohol ($C_6H_5CH_2OH$, AR), ethylene glycol (EG), ethanol, acetone and potassium hydroxide (KOH) were purchased from Sinopharm Chemical Reagent Co., Ltd The commercial Pt/C (20 wt%) and Ru/C (5%) were purchased from Alfa Aesar. The deionized water (18.2 MΩ cm^{-1}) used in all experiments was prepared by passing through an ultra-pure purification system. All chemicals and materials were used as received.

Synthesis of Ru_3Cu nanoflowers (NFs)

In a standard procedure, 12 mg of $Ru(acac)_3$, 1 mg of CuCl, 15 mg of CA, 100 mg of PVP, and 5 mL of benzyl alcohol were mixed in a 20 mL vial under magnetic stirring at room temperature for 3 h. The homogeneous mixture was then heated up to 160 °C and maintained for 3 h in an oil bath before it cooled naturally. Finally, the final product was collected by centrifugation and washed with ethanol and acetone several times. The syntheses of the Ru_2Cu NFs and Ru_6Cu NFs were conducted under the same conditions except that the amount of $Ru(acac)_3$ was varied to 8 and 24 mg, respectively.

Preparation of carbon-supported catalysts

In a standard preparation, carbon black (Vulcan XC-72) was dispersed into ethanol and sonicated for 0.5 h. The as-prepared Ru_2Cu NFs, Ru_3Cu NFs, and Ru_6Cu NFs (20 wt%) were added to this dispersion. This mixture was further stirred overnight. After that, the resultant samples were precipitated out by centrifugation and washed three times with ethanol and water. Then, the products were dried under 60 °C overnight to obtain the final catalysts.

Characterization

Transmission electron microscopy (TEM) images of the obtained samples were obtained using a HITACHI HT-7700 microscope operated at 100 kV. High-resolution transmission electron microscopy (HRTEM) was performed using an FEI Tecnai F20 G2 microscope operated at 300 kV. High-angle annular dark-field scanning TEM (HAADF-STEM) and energy dispersive X-ray (EDX) mapping analyses were obtained using an FEI Titan ChemiSTEM equipped with a probe-corrector and a Super-X EDX detector system. This microscope was operated at 200 kV with a probe current of 50 pA and a convergent angle of 21.4 mrads for illumination. The X-ray diffraction (XRD) patterns were recorded on a Miniflex600 X-ray diffractometer in a scan range of 30–90° at a scan rate of 10.0° per min. An X-ray photoelectron spectrometer (XPS) was performed on ESCALAB 250Xi (Thermo, U. K).

Electrochemical measurement

The electrochemical performances of the Ru_2Cu NFs/C, Ru_3Cu NFs/C, Ru_6Cu NFs/C, commercial Pt/C and Ru/C were measured using a three-electrode cell with a CHI760E electrochemical analyzer (CH Instrument, Shanghai) with a glassy carbon rotating disk electrode (RDE, area: ~0.196 cm^2), graphite rod, and Ag/AgCl electrode serving as the working, counter, and reference electrodes, respectively. All potentials were referenced to the reversible hydrogen electrode (RHE), and all polarization curves were corrected for the *iR* contribution within the cell. To make catalyst ink, 5 mg of the Ru_2Cu NFs/C, Ru_3Cu NFs/C, Ru_6Cu NFs/C and the commercial Pt/C and Ru/C catalysts were dispersed in 5 mL of a mixed solvent and sonicated for 10 min. The solvent contained a mixture of de-ionized water, isopropanol, and 5% Nafion 117 solution at a volumetric ratio of 8 : 2 : 0.05. 30 μL of the catalyst ink was added onto the RDE and dried under the air flow for 30 min to make the working electrode. The loading amount of the Ru_2Cu NFs/C, Ru_3Cu NFs/C, Ru_6Cu NFs/C and the commercial Pt/C and Ru/C catalysts on the RDE was determined to be ~15.3 $\mu g_{\text{Ru or Pt}}$ cm^{-2}. The electrolyte for cyclic voltammetry (CV) measurement and linear scan voltammetry (LSV) test for hydrogen evolution reaction (HER) was measured in 0.1 M KOH solution purged with pure Ar. The CV measurement was conducted in an Ar-saturated 0.1 M KOH solution at room temperature with a scan rate of 50 mV s^{-1}. Before the electrochemical measurement, the working electrode was cleaned *via* a steady-state cyclic voltammetry (CV) scan with 20 repetitions over the 0–1 V potential range (*vs.* RHE) at a scan rate of 50 mV s^{-1}. Linear sweep voltammetry (LSV) was conducted in the range of −0.4 to 0.1 V (*vs.* RHE) at a scan rate of 10 mV s^{-1} and a rotation speed of 1600 rpm to remove hydrogen gas bubbles formed on the catalyst surface. The electrochemically active surface area (ECSA) of the samples was estimated using the CV method in 0.1 M KOH at different scan rates of 20, 40, 60, 80, and 100 mV s^{-1}. The electrochemical double-layer capacitance ($C_{\rm dl}$) is from linear fitting, and the slope is the $C_{\rm dl}$ value. The ECSA of the catalyst on RDE is estimated as follows:

$$\mathrm{ECSA} = \frac{C_{\rm dl}}{C_{\rm s}} \times S,$$

where $C_{\rm s}$ is the specific capacitance of the sample and the value of $C_{\rm s}$ is estimated to be 0.04 mF cm^{-2} in this study. S is the actual surface area of the electrode, which is equal to the geometric area of the glassy carbon electrode (0.196 cm^2). The durability tests were performed by applying cyclic potential sweeps between −0.2 V and 0.1 V (*versus* reversible hydrogen electrode (*vs.* RHE)) at a scan rate of 100 mV s^{-1} for 2000 cycles. The chronoamperometry (*i*–*t*) curves were measured at the potential with the current density being nearly 10 mA cm^{-2} for 12 h.

Computational details

All the DFT calculations are performed in the framework of density functional theory using the projector-augmented plane-wave method, as implemented in the Vienna *ab initio* simulation package. The exchange–correlation potential was treated by the Perdew–Burke–Ernzerhof functional. The long-range van der Waals interaction is described by employing the DFT-D3 approach. The cut-off energy for the plane wave is set to 450 eV. The energy criterion is set to 10^{-5} eV in an iterative solution of the Kohn–Sham equation. A vacuum layer of 15 Å is added perpendicular to the sheet to avoid artificial interaction between periodic images. The 4 × 4 × 1 Monkhorst–Pack *k*-point sampling grid was used for the Brillouin zone integration. All the structures were relaxed until the residual forces on the atoms decreased to less than 0.02 eV $Å^{-1}$. The minimum energy path for each reaction step was confirmed using the nudged elastic band (NEB) method.

Results and discussion

The typical synthesis procedure of Ru_3Cu NFs is shown in Scheme 1, where Ru_3Cu NFs can be prepared by applying a facile wet chemistry method using ruthenium(III) acetylacetonate (Ru(acac)$_3$) and copper(I) chloride (CuCl) as the metal precursors, benzyl alcohol as the solvent, citric acid (CA) as the reduction agent and polyvinylpyrrolidone (PVP) as the surfactant. Ru_xCu NFs with different atomic ratios can be obtained by varying the amount of Ru(acac)$_3$ precursor fed in the synthesis. It can be found that the use of CA is crucial for the formation of unique flower-like nanostructures. As shown in Fig. S1,† only dendritic nanostructures could be obtained after replacing the CA with ascorbic acid (AA) or glucose. In addition, PVP acts as a capping agent and can effectively protect particles from aggregation. This demonstration can be supported by the TEM images; as depicted in Fig. S2a and b,† only aggregated particles can be obtained in the absence of PVP. Moreover, benzyl alcohol plays a key role in the formation of the ordered structure, replacing benzyl alcohol with ethylene glycol can lead to the formation of irregular nanoparticles (Fig. S2c and d†). Thus, Ru_3Cu NFs can be synthesized with the cooperative participation of CA, PVP and benzyl alcohol.

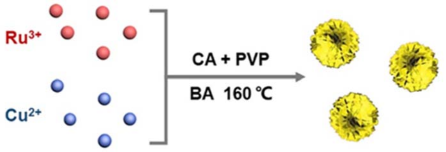

Scheme 1 Schematic illustration showing the synthetic process of the RuCu NFs.

Fig. 1 shows the morphological, structural and compositional characterizations of Ru_3Cu nanocrystals prepared by employing a standard procedure. From transmission electron microscopy (TEM, Fig. 1a) and high-angle annular dark-field scanning transmission electron microscopy (HAADF-STEM, Fig. 1b), 3D flower-like nanostructures with a homogenous distribution and high productivity were clearly observed. The average size of the flower-like nanostructure is about 44.7 nm (Fig. S3†). To further uncover the morphological and structural features of the Ru_3Cu NFs, the aberration-corrected HADDF-STEM technique was carried out. As shown in Fig. 1c and S4,† Ru_3Cu, NFs exhibit a highly opened 3D structure that comprises several ultrathin nanosheets as building blocks. Such a unique flower-like structure may endow Ru_3Cu nanocrystals with a large specific surface area and efficient mass transfer ability.[30] The magnified atomic-resolution HADDF-STEM observation (Fig. 1d) was performed to characterize the structure of sheet-like building blocks that focus on the white rectangle area, as illustrated in Fig. 1c. The lattice fringe of the nanosheet was

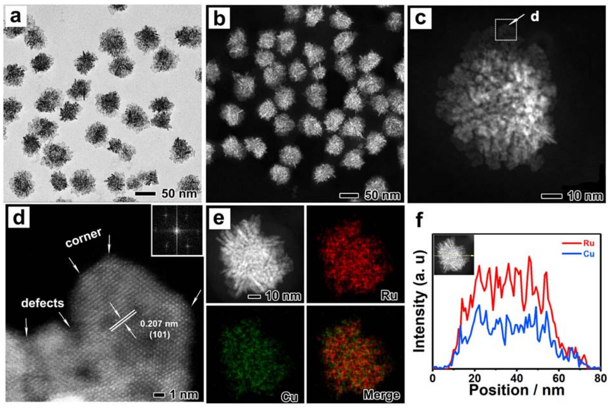

Fig. 1 (a) TEM and (b) HADDF-STEM images of the Ru_3Cu NFs. (c) HADDF-STEM image of an individual Ru_3Cu NF. (d) Atomic-resolution HADDF-STEM image at higher magnification from a selected area in (c) and the corresponding FFT pattern. (e) EDX mapping images and (f) EDX line-scan profiles of the individual Ru_3Cu NF.

measured to be 0.207 nm, which can be indexed to the {101} plane of Ru (Fig. 1d). The corresponding fast-Fourier transformation (FFT, the inset of Fig. 1d) along the [0001] axis further indicates the hexagonal-close-packed (hcp) phase of Ru_3Cu NFs and the fine crystallinity. Moreover, numerous defects, such as corners, kinks, and steps, could be observed along the edge of the nanoflowers, as marked in Fig. 1d and S4b,† which can provide additional active sites for HER. The elemental distribution of Ru and Cu in flower-like structures was characterized by energy-dispersive X-ray spectroscopy (EDX) analysis. As shown in Fig. 1e, both Ru and Cu were uniformly distributed throughout the nanoflowers, which agrees with the results of the EDX line-scan profiles (Fig. 1f). The atomic ratio of Ru/Cu was calculated to be 74.3/24.7 (Fig. S5†), which is similar to the result measured by inductively coupled plasma atomic emission spectroscopy (ICP-AES).

The crystal structure of the Ru_3Cu NFs was characterized using the X-ray diffraction (XRD) technique. As shown in Fig. 2a, all diffraction peaks of the Ru_3Cu NFs match well with those of hcp Ru (PDF # 06-0663). The lattice spacing of the (101) plane is measured to be 0.207 nm, which agrees with the HADDF-STEM results in Fig. 1d. XPS spectra were conducted to investigate the valence states and surface electron status of Ru_3Cu NFs. As shown in Fig. 2b, the strong peaks located at 461.1 and 483.4 eV correspond to the Ru^0 $3p_{3/2}$ and Ru^0 $3p_{1/2}$, indicating the majority of the metallic state in Ru. The weak peaks at 462.7 and 485.0 eV corresponding to Ru^{4+} $3p_{3/2}$ and Ru^{4+} $3p_{1/2}$ indicate that partial oxidation happened on the surface.[43] The XPS spectra of Cu 2p are shown in Fig. 2c. The peaks located at 932.5, 934.5, 952.4, and 954.5 eV can be attributed to the Cu^0 $2p_{3/2}$, Cu^{2+} $2p_{3/2}$, Cu^0 $2p_{1/2}$, and Cu^{2+} $2p_{1/2}$, respectively.[28] The peaks located at 942.1 eV are attributed to the satellite peaks. More impressively, the peaks of Ru in Ru_3Cu NFs shifted to lower binding energy when compared with commercial Ru/C (Fig. 1d and S4†). It can be concluded that Cu transferred the electrons to Ru and made Ru an electron-rich state, which might have a positive effect on the catalytic activity towards the HER by optimizing the adsorption energy of intermediates.[28,44]

Ru_2Cu and Ru_6Cu NFs were synthesized through the same procedure, except for varying the amount of Ru precursor. As can be observed from the TEM and HADDF-STEM images in Fig. S7 and S8,† Ru_2Cu NFs and Ru_6Cu NFs show the same flower-like morphologies with average sizes of 44.5 nm and 43 nm, respectively. The XRD results further indicate that they are highly crystalline with an hcp Ru phase. Lattice fringes of the {002} Ru–Cu alloy with the interplanar distances of 0.217 and 0.215 nm can be observed in the Ru_2Cu NFs and Ru_6Cu NFs, respectively (Fig. S7f and S8f†). Both EDX mapping images and line-scan profiles confirm the homogeneous distribution of Ru and Cu throughout the nanoflowers, indicating the alloys of Ru and Cu (Fig. S5 and S6†).

To investigate the catalytic abilities of HER, Ru_2Cu NFs, Ru_3Cu NFs, and Ru_6Cu NFs were first loaded onto carbon black (Vulcan X-72) for further measurement. The electrocatalytic measurements were carried out in a standard three-electrode system. The polarization curves of Ru–Cu NFs with different atomic ratios, commercial Ru/C and Pt/C were conducted in 0.1 M KOH solution. As shown in Fig. 3a, Ru_3Cu NFs possess a low overpotential of 55 mV to achieve a current density of 10

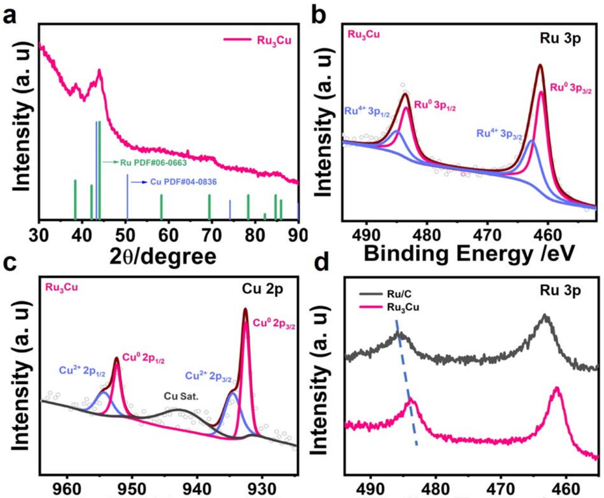

Fig. 2 (a) XRD pattern of the Ru_3Cu NFs. (b) XPS spectra of Ru 3p. (c) Cu 4p orbitals of the Ru_3Cu NFs. (d) XPS spectra of Ru 3p in the Ru/C and Ru_3Cu NFs.

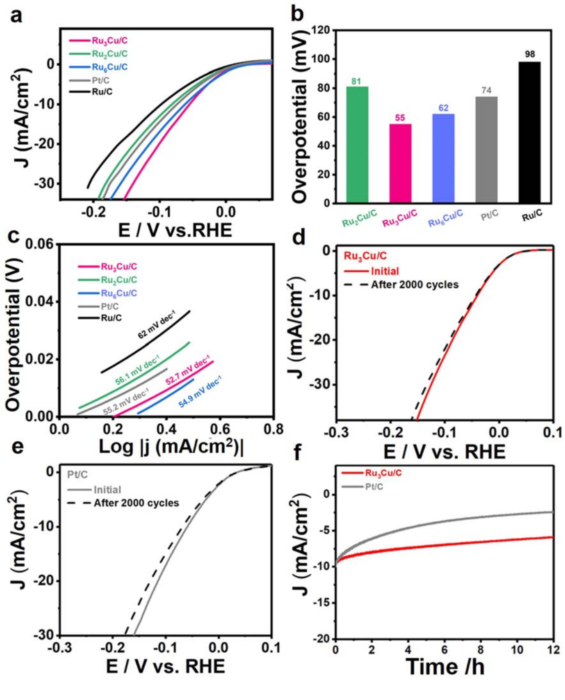

Fig. 3 (a) HER polarization curves of Ru_2Cu NFs/C, Ru_3Cu NFs/C, Ru_6Cu NFs/C, Pt/C, and Ru/C in 0.1 M KOH solution. (b) Comparison of overpotentials at a current density of 10 mA cm^{-2} with different catalysts. (c) Corresponding Tafel plots of different catalysts. (d) Polarization curves of Ru_3Cu NFs/C and (e) Pt/C before and after 2000 cyclic voltammetry cycles between −0.2 V and 0.1 V (*vs.* RHE). (f) Chronoamperometry measurements of the Ru_3Cu NFs/C and Pt/C at a potential of 10 mA cm^{-2} for 12 h.

mA cm^{-2}, which is much smaller than that of Ru_2Cu NFs/C (81 mV), Ru_6Cu NFs/C (62 mV), commercial Pt/C (74 mV), and Ru/C (98 mV) (Fig. 3b). Additionally, Ru_3Cu NFs/C present the highest activity of 33.3 mA cm^{-2} at the overpotential of −0.15 V *vs.* RHE, which is 1.5, 1.2, 1.4, and 1.8 times higher than that of Ru_2Cu NFs/C (22.7 mA cm^{-2}), Ru_6Cu NFs/C (28.6 mA cm^{-2}), Pt/C (24.3 mA cm^{-2}), and Ru/C (18.4 mA cm^{-2}) (Fig. S9†). To gain much insight into the reaction kinetics of HER, Tafel plots were derived from the polarization curves by fitting them with the Tafel equation. As shown in Fig. 3c, the Tafel slope of Ru_3Cu NFs/C is 52.7 mV dec^{-1} is much smaller than that of Ru_2Cu NFs/C (56.1 mV dec^{-1}), Ru_6Cu NFs/C (54.9 mV dec^{-1}), Pt/C (55.2 mV dec^{-1}), and Ru/C (62 mV dec^{-1}). This result indicates that the HER process on Ru_3Cu NFs/C followed the Volmer–Heyrovsky pathway with water dissociation as the rate-determining step in an alkaline solution.[45,46] In addition, the double-layer capacitances (C_{dl}) of the as-prepared catalysts were measured to evaluate the electrochemical active surface area (ECSA). As illustrated in Fig. S10 and S11,† the obtained specific capacitances for Ru_2Cu NFs/C, Ru_3Cu NFs/C, Ru_6Cu NFs/C, and Pt/C were 20.3, 18.9, 16.4 and 12.2 mF cm^{-2}, respectively, from which the ECSA value can be calculated. The larger ECSA value of Ru_3Cu NFs/C (472.5 cm^2) indicates that Ru_3Cu NFs/C can expose more active sites than Pt/C (305 cm^2). There is a volcano-like relationship toward HER performance among electrocatalysts with different Ru/Cu atomic ratios. This may be explained by the Sabatier principle, in which the proper surface electron structure states and H adsorption energy were provided in Ru_3Cu NFs.[44] In a word, it can be speculated that the optimized catalytic performance of Ru_3Cu NFs can be attributed to the opened structure and synergistic effect between Ru and Cu. However, the flower-like structure with a high density of defects and steps can provide additional active sites, and the highly opened structure is favorable for the rapid mass transfer process.[41,47,48] Obvious activity decay can be observed in Fig. S13† when substituting the flower-like structure with nanoclusters. The electron transfer occurred from Cu to Ru based on the negative shift of Ru 3p according to XPS spectra;[29,41] the ligand effect of Ru and Cu can optimize the H adsorption energy and facilitate the water dissociation process, thereby boosting HER performance.

Long-term durability is an important parameter for evaluating HER electrocatalysts. The stability of these five catalysts was evaluated through accelerated durability (ADT) for 2000 cycles between −0.2 and 0.1 V *vs.* RHE at a scan rate of 100 mV s^{-1} in an Ar-saturated 0.1 M KOH solution. Fig. 3d shows the HER polarization curves of the Ru_3Cu NFs/C before and after the test. There is no obvious change in HER polarization curves after 2000 cycles. The overpotential of Ru_3Cu NFs/C at 10 mA cm^{-2} gives only a slight increase of 4 mV in an alkaline solution, suggesting excellent stability. In contrast, Ru_2Cu NFs/C, Ru_6Cu NFs/C, Pt/C, and Ru/C perform extinguished decay with a larger overpotential increase of 7, 5, 9, and 8 mV, respectively (Fig. S12 and S14†). The long-term stability of the as-prepared Ru_3Cu NFs/C was examined using chronoamperometry (*i*–*t*) measurements. As shown in Fig. 3f, Ru_3Cu NFs/C catalysts maintain a more stable current density over 12 h, while the commercial Pt/C decreased significantly, indicating the outperforming stability of Ru_3Cu NFs/C. The morphology of Ru_3Cu NFs/C and Pt/C after the durability test were further characterized by TEM, HRTEM, EDX mapping and spectrum analyses. As shown in Fig. S15,† Ru_3Cu NFs/C still maintained the initial flower-like structure with good crystallinity, which is responsible for its outstanding durability. Moreover, EDX-spectrum analysis reveals that the Cu atoms were leached out in Ru_3Cu NFs during the catalytic reaction (from 25.7 to 13.8), which may account for the decay of HER activity after the ADT. In comparison, commercial Pt/C exhibited obvious aggregation after 2000 cycles, as shown in Fig. S16,† resulting in the considerable decay of HER properties.

To reveal the intrinsic activity enhancement toward HER, first-principle density functional theory (DFT) calculations were conducted. The structure models of Ru_3Cu, Ru and Pt are shown in Fig. 4a, where Ru_3Cu (0001), Ru (0001), and Pt (111) were cleaved as the exposing surfaces to adsorb H_2O. In alkaline media, the lack of protons makes the adsorption and cleavage of H_2O to *H and OH^- on the surface of the catalyst a critical ability for the HER process. The barrier of water dissociation may lead to insufficient H–OH cleavage and hinder HER kinetics. Thus, HER in alkaline media is governed by the intrinsic ability of the catalyst to catalyze H* to H_2 and the kinetics of water molecular dissociation. The free energy diagram of the water dissociation process is shown in Fig. 4b. After the incorporation of Cu, Ru_3Cu NFs exhibit enhanced capability with a smaller energy barrier for water dissociation relative to Ru, which agrees with the results of the lower Tafel slopes, as depicted in Fig. 3c. Moreover, models of H adsorption on the surface of Ru_3Cu, Ru and Pt are shown in Fig. 4c. The face-centered cubic (fcc) site on Ru_3Cu, fcc site on Ru and fcc site on Pt were calculated to be preferable sites in each model. The calculated free energy of the above models is shown in

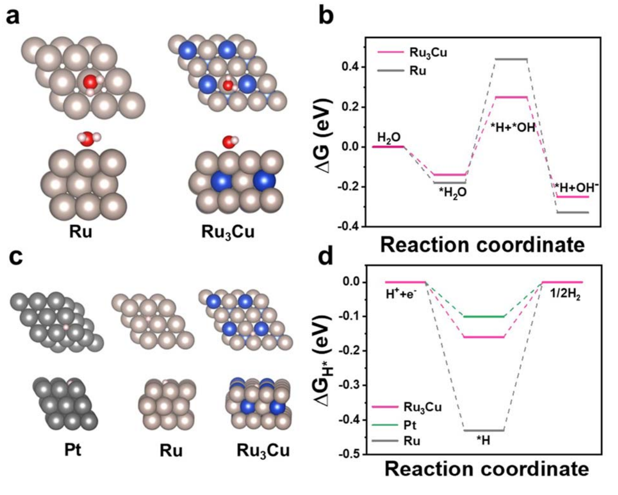

Fig. 4 Density functional theory calculation. (a) The models of adsorption H_2O on Ru and Ru_3Cu. (b) Free-energy diagram of the water dissociation process on Ru_3Cu and Ru. (c) The models of adsorption of H on the surface of Pt, Ru and Ru_3Cu. (d) Adsorption-free energies of H on Ru_3Cu, Pt and Ru.

Fig. 4b. The ΔG_{H^*} on Ru_3Cu, Ru and Pt is calculated to be −0.16, −0.43 and −0.1 eV, respectively. The ΔG_{H^*} value of Ru_3Cu NFs is close to zero, which is comparable to that of Pt, indicating the fast electron–proton transfer procedure and hydrogen desorption process. Thus, the facilitated water dissociation ability together with the optimized H adsorption/desorption ability contributes to outperforming HER performance.

Conclusions

In summary, we successfully synthesized a series of RuCu NFs by applying a facile solvothermal method. The contents of Ru and Cu can be easily modulated by varying the amounts of salt precursors. It is indicated that the RuCu NFs comprise various thin nanosheets, leading to additional active sites for HER. The incorporation of Cu significantly modified the electronic structure of Ru. Surprisingly, the overpotential of Ru_3Cu NFs at 10 mA cm^{-2} reaches only 55 mV with a Tafel slope of 52.7 mV dec^{-1}, which is superior to other Ru–Cu NFs, Ru/C and Pt/C. In addition, the Ru–Cu NFs exhibited enhanced stability for HER relative to Pt/C owing to their stable flower-like structure. DFT calculations indicate that both the facilitated water dissociation and appropriate H adsorption/desorption abilities are responsible for the outstanding catalytic performance. These findings provide a promising catalyst for HER on Ru-based catalysts, which may be applied to industrial production. This study provides a facile approach for the synthesis of 3D open nanostructures and a typical example of designing advanced Ru-based HER electrocatalysts with improved performance.

Conflicts of interest

There are no conflicts to declare.

Acknowledgements

This work was supported by the National Science Foundation of China (51871200), National Program for Support of Top-notch Young Professionals, Fundamental Research Funds for the Central Universities (226-2022-00200), and Foundation for Innovative Research Groups of the National Natural Science Foundation of China (61721005).

References

1 J. Zhu, L. Hu, P. Zhao, L. Y. S. Lee and K. Y. Wong, Recent Advances in Electrocatalytic Hydrogen Evolution Using Nanoparticles, *Chem. Rev.*, 2020, **120**(2), 851–918.

2 Y. Guo, T. Park, J. W. Yi, J. Henzie, J. Kim, Z. Wang, B. Jiang, Y. Bando, Y. Sugahara, J. Tang and Y. Yamauchi, Nanoarchitectonics for Transition-Metal-Sulfide-Based Electrocatalysts for Water Splitting, *Adv. Mater.*, 2019, **31**(17), 1807134.

3 C. Hu, L. Zhang and J. L. Gong, Recent Progress Made in the Mechanism Comprehension and Design of Electrocatalysts for Alkaline Water Splitting, *Energy Environ. Sci.*, 2019, **12**, 2620.

4 Z. Chen, X. Duan, W. Wei, S. Wang and B.-J. Ni, Recent Advances in Transition Metal-based Electrocatalysts for Alkaline Hydrogen Evolution, *J. Mater. Chem. A*, 2019, **7**(25), 14971–15005.

5 X. Wang, Y. Zheng, W. Sheng, Z. J. Xu, M. Jaroniec and S.-Z. Qiao, Strategies for Design of Electrocatalysts for Hydrogen Evolution under Alkaline Conditions, *Mater. Today*, 2020, **36**, 125–138.

6 N. Mahmood, Y. Yao, J. W. Zhang, L. Pan, X. Zhang and J. J. Zou, Electrocatalysts for Hydrogen Evolution in Alkaline Electrolytes: Mechanisms, Challenges, and Prospective Solutions, *Adv. Sci.*, 2018, **5**(2), 1700464.

7 Y. Wang, H. Zhuo, X. Zhang, X. Dai, K. Yu, C. Luan, L. Yu, Y. Xiao, J. Li, M. Wang and F. Gao, Synergistic Effect between Undercoordinated Platinum Atoms and Defective Nickel Hydroxide on Enhanced Hydrogen Evolution Reaction in Alkaline Solution, *Nano Energy*, 2018, **48**, 590–599.

8 Z. Wang, B. Xiao, Z. Lin, Y. Xu, Y. Lin, F. Meng, Q. Zhang, L. Gu, B. Fang, S. Guo and W. Zhong, $PtSe_2$/Pt Heterointerface with Reduced Coordination for Boosted Hydrogen Evolution Reaction, *Angew. Chem., Int. Ed.*, 2021, **60**(43), 23388–23393.

9 Z. Zhao, H. Liu, W. Gao, W. Xue, Z. Liu, J. Huang, X. Pan and Y. Huang, Surface-Engineered PtNi–O Nanostructure with Record-High Performance for Electrocatalytic Hydrogen Evolution Reaction, *J. Am. Chem. Soc.*, 2018, **140**(29), 9046–9050.

10 Y. Jiang, X. Wu, Y. Yan, S. Luo, X. Li, J. Huang, H. Zhang and D. Yang, Coupling PtNi Ultrathin Nanowires with MXenes for Boosting Electrocatalytic Hydrogen Evolution in Both Acidic and Alkaline Solutions, *Small*, 2019, **15**(12), 1805474.

11 I. Edezma-Yanez, W. D. Z. Wallace, P. Sebastián-Pascual, V. Climent, J. M. Feliu and M. T. M. Koper, Interfacial Water Reorganization as a pH-dependent Descriptor of the Hydrogen Evolution Rate on Platinum Electrodes, *Nat. Energy*, 2017, **2**(4), 17031.

12 X. Tian, P. Zhao and W. Sheng, Hydrogen Evolution and Oxidation: Mechanistic Studies and Material Advances, *Adv. Mater.*, 2019, **31**(31), 1808066.

13 L. Ji, P. Yan, C. Zhu, C. Ma, W. Wu, C. Wei, Y. Shen, S. Chu, J. Wang, Y. Du, J. Chen, X. Yang and Q. Xu, One-pot Synthesis of Porous 1T-phase MoS_2 Integrated with Single-atom Cu Doping for Enhancing Electrocatalytic Hydrogen Evolution Reaction, *Appl. Catal., B*, 2019, **251**, 87–93.

14 W. Liu, L. Yu, R. Yin, X. Xu, J. Feng, X. Jiang, D. Zheng, X. Gao, X. Gao, W. Que, P. Ruan, F. Wu, W. Shi and X. Cao, Non-3d Metal Modulation of a 2D Ni–Co Heterostructure Array as Multifunctional Electrocatalyst for Portable Overall Water Splitting, *Small*, 2020, **16**(10), 1906775.

15 S. Chu, W. Chen, G. Chen, J. Huang, R. Zhang, C. Song, X. Wang, C. Li and K. Ostrikov, Holey Ni–Cu Phosphide Nanosheets as a Highly Efficient and Stable Electrocatalyst for Hydrogen Evolution, *Appl. Catal., B*, 2019, **243**, 537–545.

16 Y. Shen, Y. Zhou, D. Wang, X. Wu, J. Li and J. Xi, Nickel–Copper Alloy Encapsulated in Graphitic Carbon Shells as

Electrocatalysts for Hydrogen Evolution Reaction, *Adv. Energy Mater.*, 2018, **8**(2), 1701759.

17 S.-Y. Bae, J. Mahmood, I.-Y. Jeon and J.-B. Baek, Recent Advances in Ruthenium-based Electrocatalysts for the Hydrogen Evolution Reaction, *Nanoscale Horiz.*, 2020, **5**(1), 43–56.

18 J. Creus, J. De Tovar, N. Romero, J. Garcia-Anton, K. Philippot, R. Bofill and X. Sala, Ruthenium Nanoparticles for Catalytic Water Splitting, *ChemSusChem*, 2019, **12**(12), 2493–2514.

19 B. Lu, L. Guo, F. Wu, Y. Peng, J. E. Lu, T. J. Smart, N. Wang, Y. Z. Finfrock, D. Morris, P. Zhang, N. Li, P. Gao, Y. Ping and S. Chen, Ruthenium Atomically Dispersed in Carbon Outperforms Platinum toward Hydrogen Evolution in Alkaline Media, *Nat. Commun.*, 2019, **10**(1), 631.

20 Z. Zhang, H. Wang, M. Ma, H. Liu, Z. Zhang, W. Zhou and H. Liu, Integrating NiMoO Wafer as a Heterogeneous 'Turbo' for Engineering Robust Ru-based Electrocatalyst for Overall Water Splitting, *Chem. Eng. J.*, 2021, **420**, 127686.

21 Z. Zhuang, Y. Wang, C. Q. Xu, S. Liu, C. Chen, Q. Peng, Z. Zhuang, H. Xiao, Y. Pan, S. Lu, R. Yu, W. C. Cheong, X. Cao, K. Wu, K. Sun, Y. Wang, D. Wang, J. Li and Y. Li, Three-dimensional Open Nano-netcage Electrocatalysts for Efficient pH-Universal Overall Water Splitting, *Nat. Commun.*, 2019, **10**(1), 4875.

22 Y. Liu, X. Li, Q. Zhang, W. Li, Y. Xie, H. Liu, L. Shang, Z. Liu, Z. Chen, L. Gu, Z. Tang, T. Zhang and S. Lu, A General Route to Prepare Low-Ruthenium-Content Bimetallic Electrocatalysts for pH-Universal Hydrogen Evolution Reaction by Using Carbon Quantum Dots, *Angew. Chem., Int. Ed.*, 2020, **59**(4), 1718–1726.

23 W. Lai, P. Yu, L. Gao, Z. Yang, B. He and H. Huang, Boosting the Interfacial Hydrogen Migration for Efficient Alkaline Hydrogen Evolution on Pt-based Nanowires, *J. Mater. Chem. A*, 2022, **10**(32), 16834–16841.

24 Y. Li, L. Zhang, Y. Qin, F. Chu, Y. Kong, Y. Tao, Y. Li, Y. Bu, D. Ding and M. Liu, Crystallinity Dependence of Ruthenium Nanocatalyst toward Hydrogen Evolution Reaction, *ACS Catal.*, 2018, **8**, 5714–5720.

25 S. Okazoe, K. Kusada, D. Wu, T. Yamamoto, T. Toriyama, S. Matsumura, S. Kawaguchi, Y. Kubota and H. Kitagawa, Synthesis of Mo and Ru solid-solution Alloy NPs and Their Hydrogen Evolution Reaction Activity, *Chem. Commun.*, 2020, **56**(92), 14475–14478.

26 G. Liu, W. Zhou, B. Chen, Q. Zhang, X. Cui, B. Li, Z. Lai, Y. Chen, Z. Zhang, L. Gu and H. Zhang, Synthesis of RuNi Alloy Nanostructures Composed of Multilayered Nanosheets for Highly Efficient Electrocatalytic Hydrogen Evolution, *Nano Energy*, 2019, **66**, 104173.

27 J. Mao, C. T. He, J. Pei, W. Chen, D. He, Y. He, Z. Zhuang, C. Chen, Q. Peng, D. Wang and Y. Li, Accelerating Water Dissociation Kinetics by Isolating Cobalt Atoms into Ruthenium Lattice, *Nat. Commun.*, 2018, **9**(1), 4958.

28 D. Cao, J. Wang, H. Xu and D. Cheng, Growth of Highly Active Amorphous RuCu Nanosheets on Cu Nanotubes for the Hydrogen Evolution Reaction in wide pH values, *Small*, 2020, **16**(37), 2000924.

29 Q. Wu, M. Luo, J. Han, W. Peng, Y. Zhao, D. Chen, M. Peng, J. Liu, F. M. F. de Groot and Y. Tan, Identifying Electrocatalytic Sites of the Nanoporous Copper–Ruthenium Alloy for Hydrogen Evolution Reaction in Alkaline Electrolyte, *ACS Energy Lett.*, 2019, **5**(1), 192–199.

30 Q. Yao, B. Huang, N. Zhang, M. Sun, Q. Shao and X. Huang, Channel-Rich RuCu Nanosheets for pH-Universal Overall Water Splitting Electrocatalysis, *Angew. Chem., Int. Ed.*, 2019, **58**(39), 13983–13988.

31 Y. Shi, Z. Lyu, M. Zhao, R. Chen, Q. N. Nguyen and Y. Xia, Noble-Metal Nanocrystals with Controlled Shapes for Catalytic and Electrocatalytic Applications, *Chem. Rev.*, 2021, **121**(2), 649–735.

32 C. Xiao, B.-A. Lu, P. Xue, N. Tian, Z.-Y. Zhou, X. Lin, W.-F. Lin and S.-G. Sun, High-index-facet and High-surface-energy Nanocrystals of Metals and Metal Oxides as Highly Efficient Catalysts, *Joule*, 2020, **4**(12), 2562–2598.

33 A. R. Poerwoprajitno, L. Gloag, S. Cheong, J. J. Gooding and R. D. Tilley, Synthesis of Low- and High-index Faceted Metal (Pt, Pd, Ru, Ir, Rh) Nanoparticles for Improved Activity and Stability in Electrocatalysis, *Nanoscale*, 2019, **11**(41), 18995–19011.

34 Y. Wang, H. Zhuo, X. Zhang, X. Dai, K. Yu, C. Luan, L. Yu, Y. Xiao, J. Li, M. Wang and F. Gao, Synergistic Effect Between Undercoordinated Platinum Atoms and Defective Nickel Hydroxide on Enhanced Hydrogen Evolution Reaction in Alkaline Solution, *Nano Energy*, 2018, **48**, 590–599.

35 F. Lv, W. Zhang, M. Sun, F. Lin, T. Wu, P. Zhou, W. Yang, P. Gao, B. Huang and S. Guo, Au Clusters on Pd Nanosheets Selectively Switch the Pathway of Ethanol Electrooxidation: Amorphous/Crystalline Interface Matters, *Adv. Energy Mater.*, 2021, **11**(19), 2100187.

36 Y. Lu, H. Zhang, H. Liu, Z. Nie, F. Xu, Y. Zhao, J. Zhu and W. Huang, Electrolyte Dynamics Engineering for Flexible Fiber-Shaped Aqueous Zinc-Ion Battery with Ultralong Stability, *Nano Lett.*, 2021, **21**, 9651–9660.

37 K. Liang, A. Tabassum, M. Kothakonda, X. Zhang, R. Zhang, B. Kenney, B. D. Koplitz, J. Sun and M. Naguib, Two-dimensional Titanium Carbonitride MXene as a Highly Efficient Electrocatalyst for Hydrogen Evolution Reaction, *Mater. Rep. Energy*, 2022, **2**(1), 100075.

38 M. Gong, F. Li, Z. Yao, S. Zhang, J. Dong, Y. Chen and Y. Tang, Highly Active and Durable Platinum–lead Bimetallic Alloy Nanoflowers for Formic Acid Electrooxidation, *Nanoscale*, 2015, **7**(11), 4894–4899.

39 H. Y. Chen, H. J. Niu, X. Ma, J. J. Feng, X. Weng, H. Huang and A. J. Wang, Flower-like Platinum–Cobalt–Ruthenium Alloy Nanoassemblies as Robust and Highly Efficient Electrocatalyst for Hydrogen Evolution Reaction, *J. Colloid Interface Sci.*, 2020, **561**, 372–378.

40 N. Fernando, J. Swaminathan, F. Hernandez, G. Priyadarshana, C. Sandaruwan, W. Yang, V. Karunaratne, Z. Wang, G. Amaratunga, N. Kottegoda, A. Meiyazhagan and P. Ajayan, Pseudobrookite Based Heterostructures for Efficient Electrocatalytic Hydrogen Evolution, *Mater. Rep. Energy*, 2021, **1**(2), 100020.

41 B. Ma, P. Y. Guan, Q. Y. Li, M. Zhang and S. Q. Zang, MOF-derived Flower-like MoS_2@TiO_2 Nanohybrids with Enhanced Activity for Hydrogen Evolution, *ACS Appl. Mater. Interfaces*, 2016, **8**(40), 26794–26800.

42 D. Chen, R. Lu, Z. Pu, J. Zhu, H.-W. Li, F. Liu, S. Hu, X. Luo, J. Wu, Y. Zhao and S. Mu, Ru-doped 3D Flower-like Bimetallic Phosphide with a Climbing Effect on Overall Water Splitting, *Appl. Catal., B*, 2020, **279**, 119396.

43 J. Tang, B. Wang, Y. Zhang, X. Zhang, Q. Shen, J. Qin, S. Xue, X. Guo, C. Du and J. Chen, One-step Integration of Amorphous RuB_x and Crystalline Ru Nanoparticles into B/N-doped Porous Carbon Polyhedra for Robust Electrocatalytic Activity Towards the HER in both Acidic and Basic Media, *J. Mater. Chem. A*, 2022, **10**, 4181–4190.

44 F. Lv, W. Zhang, W. Yang, J. Feng, K. Wang, J. Zhou, P. Zhou and S. Guo, Ir-Based Alloy Nanoflowers with Optimized Hydrogen Binding Energy as Bifunctional Electrocatalysts for Overall Water Splitting, *Small Methods*, 2019, **4**(6), 1900129.

45 X. Feng, Y. Shi, J. Shi, L. Hao and Z. Hu, Superhydrophilic 3D Peony Flower-like Mo-doped Ni_2S_3@NiFe LDH Heterostructure Electrocatalyst for Accelerating Water Splitting, *Int. J. Hydrogen Energy*, 2021, **46**(7), 5169–5180.

46 J. Liang, L. Zhu, S. Chen, C. Priest, X. Liu, H. L. Wang, G. Wu and Q. Li, Defect-Rich Copper-doped Ruthenium Hollow Nanoparticles for Efficient Hydrogen Evolution Electrocatalysis in Alkaline Electrolyte, *Chem.–Asian J.*, 2020, **15**(18), 2868–2872.

47 R. Ojani, E. Hasheminejad and J. B. Raoof, Direct Growth of 3D Flower-like Pt Nanostructures by a Template-free Electrochemical Route as an Efficient Electrocatalyst for Methanol Oxidation Reaction, *Energ*, 2015, **90**, 1122–1131.

48 S. Luo, Y. Ou, L. Li, J. Li, X. Wu, Y. Jiang, M. Gao, X. Yang, H. Zhang and D. Yang, Intermetallic Pd_3Pb Ultrathin Nanoplate-constructed Flowers with Low-Coordinated Edge Sites Boost Oxygen Reduction Performance, *Nanoscale*, 2019, **11**, 17301–17307.